

Hybrid Spatio-Spectral Total Variation: A Regularization Technique for Hyperspectral Image Denoising and Compressed Sensing

Saori Takeyama, *Student Member, IEEE*, Shunsuke Ono, Itsuo Kumazawa, *Member, IEEE*

Abstract—We propose a new regularization technique, named Hybrid Spatio-Spectral Total Variation (HSSTV), for hyperspectral (HS) image denoising and compressed sensing. Regularization techniques based on total variation (TV) focus on local differences of an HS image to model its underlying smoothness and have been recognized as a popular approach to HS image restoration. However, existing TVs do not fully exploit underlying spectral correlation in their designs and/or require a high computational cost in optimization. Our HSSTV is designed to simultaneously evaluate two types of local differences: direct local spatial differences and local spatio-spectral differences in a unified manner with a balancing weight. This design resolves the said drawbacks of existing TVs. Then, we formulate HS image restoration as a constrained convex optimization problem involving HSSTV and develop an efficient algorithm based on the alternating direction method of multipliers (ADMM) for solving it. In the experiments, we illustrate the advantages of HSSTV over several state-of-the-art methods.

Index Terms—hyperspectral image restoration, total variation, ADMM, denoising, compressed sensing.

I. INTRODUCTION

HYPERSPECTRAL (HS) images are required with many applications in a wide range of field, e.g., earth observation, agriculture, and medical and biological imaging [1]–[3]. An HS image has 1D spectral information including invisible light and narrow wavelength interval in addition to 2D spatial information and thus can visualize invisible intrinsic characteristics of scene objects and environmental lighting.

Observed HS images are often affected by noise because of the small amount of light in narrow wavelength and/or sensor failure. Also, in compressive HS imaging [4], [5], we have to estimate a full HS image from incomplete measurements. Thus, we need some methods for restoring clean HS images in HS applications.

Most HS image restoration methods are established based on optimization: a restored HS image is characterized as a

solution to some optimization problem, which consists of regularization and data-fidelity terms. The regularization term plays a role to incorporate a-priori knowledge about underlying properties on HS images, and so the design is very important to get a reasonable result under ill-posed or ill-conditioned scenarios, which is typical in HS image restoration.

Regularization techniques based on total variation (TV) have been recognized as a powerful approach to image restoration. Since natural images have piecewise-smooth structures, the total magnitude of local spatial differences tends to be small. Hyperspectral TV (HTV) [6], its band-group-wise extension [8], and collaborative TV (CTV) [7] are relatively simple TV regularization techniques for HS images. These TVs strongly promote spatial piecewise-smoothness, but they do not or a little care about spectral correlation, which is a typical property of HS images. As a result, these TVs cause spatial oversmoothing, as will be detailed in Sec. III. Some TVs rely on semilocal [9], [10] or nonlocal [11], [12] similarity of HS images. Although they can remove noise while keeping sharp edges, the use of them often results in spectral distortion because of ignoring spectral correlation.¹

To overcome the drawback in the above TVs, there have been proposed many methods that explicitly take spectral correlation into account. Such methods can be roughly classified into two approaches: (i) combining the above TVs with low-rank modeling (LRM), and (ii) incorporating spectral correlation into the design of TV.

The methods proposed in [10], [16]–[18] are categorized as the approach (i), which characterize spectral correlation via low-rankness. They can restore better HS images than the methods only using the above TVs. However, their computational cost is expensive because one has to compute iterative singular value decomposition in optimization involving LRM. Moreover, since TV and LRM are different types of regularization terms, tuning of hyperparameters is difficult in their models.

Arranged structure tensor TV (ASTV) [13], spatio-spectral TV (SSTV) [14], and anisotropic SSTV (ASSTV) [15] are categorized as (ii), which explicitly evaluate spectral correlation in addition to spatial piecewise-smoothness. ASTV models spectral correlation as the low-rankness of semilocal gradient matrices. However, the use of ASTV requires singular value decomposition as with LRM, and so the computational cost

Manuscript received xx xxx, 2019; revised xx xxx, 2019; accepted xx xxx, 2019.

S. Takeyama is with the Department of Information and Communications Engineering, Tokyo Institute of Technology, Kanagawa, 226-8503, Japan, email: takeyama.s.aa@m.titech.ac.jp (see <https://sites.google.com/view/saori-takeyama/home>).

S. Ono is with the School of Computing, Tokyo Institute of Technology, Kanagawa 226-8503, Japan.

I. Kumazawa is with the Institute of Innovative Research (IIR), Tokyo Institute of Technology, Kanagawa 226-8503, Japan.

Color versions of one or more of the figures in this paper are available online at <http://ieeexplore.ieee.org>.

Digital Object Identifier xx.xxxx/TGRS.2019.xxxxxxx

¹In addition, TVs based on nonlocal similarity require a chicken-and-egg self-similarity evaluation for finding similar patches.

TABLE I
THE FEATURE OF EXISTING REGULARIZATION TECHNIQUES FOR HS IMAGE.

feature methods	spatial smoothness	spectral correlation	gradient locality	hyperparameter setting	computational cost
HTV [6], CTV [7] and SRBFuse [8]	○	×	local	easy	○
STTV [9]	○	×	semilocal	easy	×
LRWTV [10]	○	△	semilocal	easy	△
NLSTTV [11]	○	×	nonlocal	easy	×
NLTV [12]	○	×	nonlocal	easy	×
ASTV [13]	○	○	semilocal	easy	×
SSTV [14]	△	○	local	easy	○
ASSTV [15]	○	○	local	difficult	○
HTV + LRM [16]–[18]	○	○	local	difficult	×
LRWTV + LRM [10]	○	○	semilocal	difficult	×
ASSTV + LRM [15]	○	○	local	difficult	×
SSTV + LRM [19]–[23]	△	○	local	difficult	×
HSSTV	○	○	local	easy	○

becomes high. On the other hand, in the design of SSTV and ASSTV, spatial correlation is interpreted as spectral piecewise-smoothness and is evaluated by the ℓ_1 norm of local differences along a spectral direction, resulting in computationally efficient optimization. Specifically, to evaluate spatial and spectral piecewise-smoothness simultaneously, SSTV focuses on local spatio-spectral differences. However, it ignores direct local spatial differences, and so restored HS images by SSTV tend to have artifacts, especially in highly noisy scenarios. Meanwhile, ASSTV directly handles both local spatial and spectral differences in parallel, but it often produces spectral oversmoothing because it strongly suppresses the ℓ_1 norm of direct spectral differences (SSTV and ASSTV are detailed in Sec. III). Some methods [15], [19]–[23] combine SSTV/ASSTV with LRM, but their computational cost is expensive due to LRM. Table I summarizes the pros and cons of the methods reviewed in this section.

Based on the above discussion, we propose a new TV regularization technique for HS image restoration, named Hybrid Spatio-Spectral Total Variation (HSSTV). To effectively utilize a-priori knowledge on HS images, HSSTV is designed to evaluate two types of local differences: direct local spatial differences and local spatio-spectral differences in a unified manner with a balancing weight. This design resolves the drawbacks of the existing TV regularization techniques mentioned above. HSSTV consists of local difference operators and the ℓ_1 /mixed $\ell_{1,2}$ norm, and thus optimization problems involving HSSTV can be efficiently solved by nonsmooth convex optimization methods like proximal splitting algorithms. Specifically, we develop an algorithm based on the alternating direction method of multipliers (ADMM) [24]–[27].

The remainder of the paper is organized as follows. Section II introduces notation and mathematical ingredients. Section III reviews existing work related to our method. In Section IV, we establish HSSTV, formulate HS image restoration as a nonsmooth convex optimization problem involving HSSTV, and develop an algorithm for solving the problem. Extensive experiments on denoising and compressed sensing (CS) reconstruction of HS images are given in Section V, where we illustrate the advantages of HSSTV over several state-of-the-art methods. Section VI concludes the paper. The preliminary

version of this work, without mathematical details, deeper discussion, new applications, and comprehensive experiments has appeared in conference proceedings [28].

II. PRELIMINARIES

A. Notation and Definitions

In this paper, let \mathbb{R} be the set of real numbers. We shall use boldface lowercase and capital to represent vectors and matrices, respectively, and $:=$ to define something. We denote the transpose of a vector/matrix by $(\cdot)^\top$, and the Euclidean norm (the ℓ_2 norm) of a vector by $\|\cdot\|$.

For notational convenience, we treat an HS image $\mathcal{U} \in \mathbb{R}^{N_v \times N_h \times B}$ as a vector $\mathbf{u} \in \mathbb{R}^{NB}$ ($N := N_v N_h$ is the number of the pixels of each band, and B is the number of the bands) by stacking its columns on top of one another, i.e., the index of the component of the i th pixel in k th band is $i + (k-1)N$ (for $i = 1, \dots, N$ and $k = 1, \dots, B$).

B. Proximal Tools

A function $f : \mathbb{R}^L \rightarrow (-\infty, \infty]$ is called *proper lower semicontinuous convex* if $\text{dom}(f) := \{\mathbf{x} \in \mathbb{R}^L \mid f(\mathbf{x}) < \infty\} \neq \emptyset$, $\text{lev}_{\leq \alpha}(f) := \{\mathbf{x} \in \mathbb{R}^L \mid f(\mathbf{x}) \leq \alpha\}$ is closed for every $\alpha \in \mathbb{R}$, and $f(\lambda \mathbf{x} + (1-\lambda)\mathbf{y}) \leq \lambda f(\mathbf{x}) + (1-\lambda)f(\mathbf{y})$ for every $\mathbf{x}, \mathbf{y} \in \mathbb{R}^L$ and $\lambda \in (0, 1)$, respectively. Let $\Gamma_0(\mathbb{R}^L)$ be the set of all proper lower semicontinuous convex functions on \mathbb{R}^L .

The *proximity operator* [29] plays a central role in convex optimization based on proximal splitting. The proximity operator of $f \in \Gamma_0(\mathbb{R}^L)$ with an index $\gamma > 0$ is defined by

$$\text{prox}_{\gamma f}(\mathbf{x}) := \underset{\mathbf{y}}{\text{argmin}} f(\mathbf{y}) + \frac{1}{2\gamma} \|\mathbf{y} - \mathbf{x}\|^2.$$

We introduce the indicator function of a nonempty closed convex set $C \subset \mathbb{R}^L$, which is defined as follows:

$$\iota_C(\mathbf{x}) := \begin{cases} 0, & \text{if } \mathbf{x} \in C, \\ \infty, & \text{otherwise.} \end{cases}$$

Then, for any $\gamma > 0$, its proximity operator is given by

$$\text{prox}_{\gamma \iota_C}(\mathbf{x}) = P_C(\mathbf{x}) := \underset{\mathbf{y} \in C}{\text{argmin}} \|\mathbf{x} - \mathbf{y}\|,$$

where $P_C(\mathbf{x})$ is the metric projection onto C .

C. Alternating Direction Method of Multipliers (ADMM)

ADMM [24]–[27] is a popular proximal splitting method, and it can solve convex optimization problems of the form:

$$\min_{\mathbf{x}, \mathbf{z}} f(\mathbf{x}) + g(\mathbf{z}) \text{ s.t. } \mathbf{z} = \mathbf{G}\mathbf{x}, \quad (1)$$

where $f \in \Gamma_0(\mathbb{R}^{L_1})$, $g \in \Gamma_0(\mathbb{R}^{L_2})$, and $\mathbf{G} \in \mathbb{R}^{L_2 \times L_1}$. Here, we assume that f is quadratic, g is *proximable*, i.e., the proximity operator of g is computable in an efficient manner, and \mathbf{G} is a full-column rank matrix. For arbitrarily chosen $\mathbf{z}^{(0)}$, $\mathbf{d}^{(0)}$ and a step size $\gamma > 0$, ADMM iterates the following steps:

$$\begin{cases} \mathbf{x}^{(n+1)} = \underset{\mathbf{x}}{\operatorname{argmin}} f(\mathbf{x}) + \frac{1}{2\gamma} \|\mathbf{z}^{(n)} - \mathbf{G}\mathbf{x} - \mathbf{d}^{(n)}\|^2, \\ \mathbf{z}^{(n+1)} = \operatorname{prox}_{\gamma g}(\mathbf{G}\mathbf{x}^{(n+1)} + \mathbf{d}^{(n)}), \\ \mathbf{d}^{(n+1)} = \mathbf{d}^{(n)} + \mathbf{G}\mathbf{x}^{(n+1)} - \mathbf{z}^{(n+1)}, \end{cases} \quad (2)$$

A convergence property of ADMM is given as follows.

Theorem 1 (Convergence of ADMM [26]). *Consider Prob. (1), and assume that $\mathbf{G}^\top \mathbf{G}$ is invertible and that a saddle point of its unaugmented Lagrangian $\mathcal{L}_0(\mathbf{x}, \mathbf{z}, \mathbf{y}) := f(\mathbf{x}) + g(\mathbf{z}) - \langle \mathbf{y}, \mathbf{G}\mathbf{x} - \mathbf{z} \rangle$ exists.² Then the sequence $(\mathbf{x}_n)_{n>0}$ generated by (2) converges to an optimal solution to Prob. (1).*

III. RELATED WORKS

In this section, we elaborate on existing local TVs for HS images, which are closely related to our TV.

Yuan *et al.* proposed HTV [6] for HS image denoising. HTV can be seen as a generalization of the standard color TV [30], and its formulation is given as follows:

$$\text{HTV}(\mathbf{u}) := \sum_{i=1}^N \sqrt{\sum_{j=1}^B (d_{v,ij}^2 + d_{h,ij}^2)},$$

where $d_{v,ij}$ and $d_{h,ij}$ are vertical and horizontal differences for i th pixel of j th band in an HS image, respectively. From this definition, one can see that HTV evaluates spatial piecewise-smoothness but does not consider spectral correlation, resulting in spatial oversmoothing. This will be empirically shown in Sec. V

Addesso *et al.* proposed to use CTV [31] for HS image inpainting [7]. CTV is defined by

$$\text{CTV}(\mathbf{u}) := \left(\sum_{i=1}^N \left(\sum_{j=1}^B (|d_{v,ij}|^p + |d_{h,ij}|^p)^{\frac{q}{p}} \right)^{\frac{r}{q}} \right)^{\frac{1}{r}}.$$

It evaluates spatial piecewise-smoothness by using $\ell_{p,q,r}$ norm. In addition, the method can also use the Schatten- p norm as

$$\text{CTV}(\mathbf{u}) := \left(\sum_{i=1}^N \left\| \begin{pmatrix} d_{v,i1} & \cdots & d_{v,iB} \\ d_{h,i1} & \cdots & d_{h,iB} \end{pmatrix} \right\|_{S_p}^q \right)^{\frac{1}{q}}.$$

CTV can be seen as a generalization of HTV, which is equivalent to HTV when $p = 2$, $q = 2$ and $r = 1$. In [7],

² A triplet $(\hat{\mathbf{x}}, \hat{\mathbf{z}}, \hat{\mathbf{d}})$ is a saddle point of an unaugmented Lagrangian \mathcal{L}_0 if and only if $\mathcal{L}_0(\hat{\mathbf{x}}, \hat{\mathbf{z}}, \hat{\mathbf{d}}) \leq \mathcal{L}_0(\mathbf{x}, \hat{\mathbf{z}}, \hat{\mathbf{d}}) \leq \mathcal{L}_0(\mathbf{x}, \mathbf{z}, \hat{\mathbf{d}})$, for any $(\mathbf{x}, \mathbf{z}, \mathbf{d}) \in \mathbb{R}^{L_1} \times \mathbb{R}^{L_2} \times \mathbb{R}^{L_2}$.

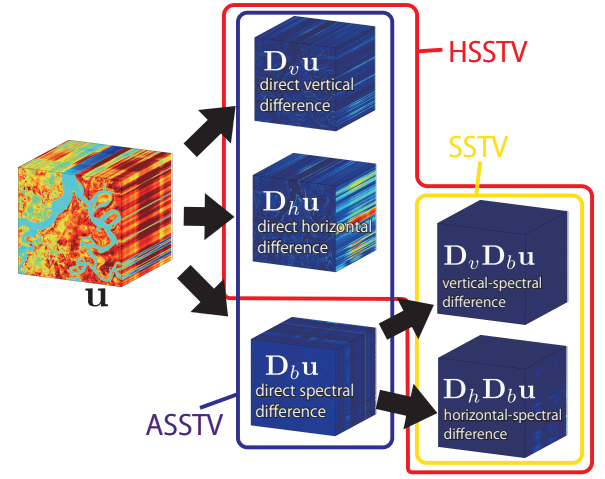


Fig. 1. Calculation of local differences in SSTV, ASSTV and our HSSTV. SSTV evaluates the ℓ_1 norm of spatio-spectral differences (yellow lines). ASSTV evaluates the ℓ_1 norm of direct spatial and spectral differences (blue lines). HSSTV evaluates the mixed $\ell_{1,p}$ norm of both direct spatial and spatio-spectral differences (red lines).

the authors experimentally show that CTV with $\ell_{2,2,1}$ norm achieves the best performance, which means that the limitation of CTV in HS image restoration is the same as HTV.

He *et al.* proposed ASSTV [15] for HS image denoising. ASSTV simultaneously evaluates direct spatial differences and direct spectral differences, which is defined by

$$\text{ASSTV}(\mathbf{u}) := \sum_{i=1}^{NB} \|(\tau_v d_{v,i}, \tau_h d_{h,i}, \tau_b d_{b,i})\|_1,$$

where $d_{v,i}$, $d_{h,i}$, and $d_{b,i}$ are vertical, horizontal, and spectral differences for the i th pixel of an HS image, respectively, and τ_v , τ_h and $\tau_b > 0$ are balancing parameters for each difference (Fig. 1, blue lines). ASSTV evaluates three direct differences in parallel but extremely suppress essential variation in spectral direction. As a result, the results by ASSTV are spectral oversmoothing even if τ_v , τ_h , and τ_b are set as suitable values (see the graphs (d) of Fig. 5 and 9). Moreover, although the parameters play a very important role, their suitable values are changed for each HS image and noise intensity. Therefore, their settings are very difficult.

Aggarwal and Majumder proposed SSTV [14] for HS image denoising, which is defined as follows:

$$\text{SSTV}(\mathbf{u}) := \sum_{i=1}^{NB} \|(d_{vb,i}, d_{hb,i})\|_1, \quad (3)$$

where $d_{vb,i}$ and $d_{hb,i}$ are vertical-spectral and horizontal-spectral differences for i th pixel of the HS image, respectively. SSTV considers spectral piecewise-smoothness of HS images together with spatial piecewise-smoothness. Specifically, in (3), local spectral differences of an HS image are calculated before the calculation of local spatial differences (Fig. 1, yellow lines). SSTV is an effective and computationally efficient regularization technique for HS image restoration, and outperforms several popular regularization methods that are

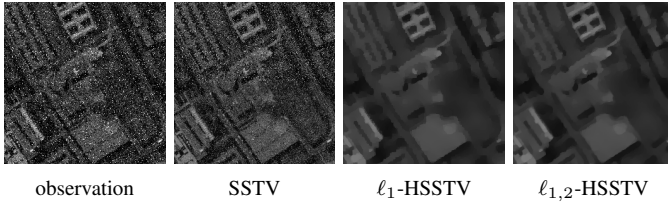


Fig. 2. Restored HS images from an observation contaminated by similar noise in adjacent bands (the upper half area) and random noise (the lower half area).

not limited to TVs [6], [32]–[34]. However, SSTV cannot remove similar noise in adjacent bands because of the definition of the spatio-spectral differences. Therefore, it often causes undesirable spatial artifacts, as will be demonstrated in Sec. V.

IV. PROPOSED METHOD

A. Hybrid Spatio Spectral Total Variation

Now, we propose a new regularization technique for HS image restoration, named HSSTV. Our TV simultaneously handles both direct local spatial differences and local spatio-spectral differences of an HS image. Here, \mathbf{D}_v , \mathbf{D}_h , and \mathbf{D}_b are vertical, horizontal, and spectral difference operators, respectively, and we denote a local spatial difference operator as $\mathbf{D} = (\mathbf{D}_v^\top \mathbf{D}_h^\top)^\top \in \mathbb{R}^{2NB \times NB}$. Then, HSSTV is defined by

$$\text{HSSTV}(\mathbf{u}) := \|\mathbf{A}_\omega \mathbf{u}\|_{1,p} \text{ with } \mathbf{A}_\omega := \begin{pmatrix} \mathbf{D} \mathbf{D}_b \\ \omega \mathbf{D} \end{pmatrix}, \quad (4)$$

where $\|\cdot\|_{1,p}$ is the mixed $\ell_{1,p}$ norm, and $\omega \geq 0$. We assume $p = 1$ or 2 , i.e., the ℓ_1 norm ($\|\cdot\|_{1,1} = \|\cdot\|_1$) or the mixed $\ell_{1,2}$ norm, respectively.

In (4), $\mathbf{D} \mathbf{D}_b \mathbf{u}$ and $\mathbf{D} \mathbf{u}$ correspond to local spatio-spectral and direct local spatial differences, respectively, as shown in Fig. 1 (red lines). The weight ω adjusts the relative importance of direct spatial piecewise-smoothness to spatio-spectral piecewise-smoothness. HSSTV evaluates two kinds of smoothness by taking the ℓ_p norm ($p = 1$ or 2) of these differences associated with each pixel and then summing up for all pixels, i.e., calculating the ℓ_1 norm. Thus, it can be defined via the mixed $\ell_{1,p}$ norm. When we set $\omega = 0$ and $p = 1$, HSSTV recovers SSTV as (3), meaning that HSSTV can be seen as a generalization of SSTV.

As reviewed in Sec. III, since SSTV only evaluates spatio-spectral piecewise-smoothness, it cannot remove similar noise in adjacent bands. The direct spatial differences in HSSTV help to remove such noise. Fig. 2 is restored HS images from an observation contaminated by similar noise in adjacent bands (the upper half area) and random noise (the lower half area). One can see that large noise remains in the upper half area of the result by SSTV. In contrast, HSSTV effectively removes all noise. However, since minimizing the direct spatial differences strongly promotes spatial piecewise-smoothness, HSSTV produces spatial oversmoothing when the weight ω is large. Thus, the weight ω should be set to less than one, as will be demonstrated in Sec. V.

B. HS Image Restoration by HSSTV

We consider to restore a clean HS image $\bar{\mathbf{u}} \in \mathbb{R}^{NB}$ from an observation $\mathbf{v} \in \mathbb{R}^M$ ($M \leq NB$) contaminated by a gaussian-sparse mixed noise, where sparse noise $\mathbf{s} \in \mathbb{R}^M$ corrupts only few pixels in the HS image but heavily, e.g., impulse noise, salt-and-pepper noise, and line noise. The observation model is given by the following form:

$$\mathbf{v} = \Phi \bar{\mathbf{u}} + \mathbf{n} + \mathbf{s}, \quad (5)$$

where $\Phi \in \mathbb{R}^{M \times NB}$ is a matrix representing a linear observation process, e.g., random sampling and $\mathbf{n} \in \mathbb{R}^M$ is a Gaussian noise with the standard deviation σ .

Based on the above model, we formulate HS image restoration using HSSTV as the following optimization problem:

$$\begin{aligned} \min_{\mathbf{u}, \mathbf{s}} \quad & \text{HSSTV}(\mathbf{u}) \\ \text{s.t.} \quad & \begin{cases} \Phi \mathbf{u} + \mathbf{s} \in \mathcal{B}_{2,\varepsilon}^{\mathbf{v}} := \{\mathbf{x} \in \mathbb{R}^M \mid \|\mathbf{v} - \mathbf{x}\| \leq \varepsilon\}, \\ \mathbf{s} \in \mathcal{B}_{1,\eta} := \{\mathbf{x} \in \mathbb{R}^M \mid \|\mathbf{x}\|_1 \leq \eta\}, \\ \mathbf{u} \in [\mu_{\min}, \mu_{\max}]^{NB}, \end{cases} \end{aligned} \quad (6)$$

where $\mathcal{B}_{2,\varepsilon}^{\mathbf{v}}$ is a \mathbf{v} -centered ℓ_2 -norm ball with the radius $\varepsilon > 0$, $\mathcal{B}_{1,\eta}$ is a $\mathbf{0}$ -centered ℓ_1 -norm ball with the radius $\eta > 0$, and $[\mu_{\min}, \mu_{\max}]^{NB}$ is a dynamic range of an HS image ($\mu_{\min} < \mu_{\max}$). This method simultaneously estimates the clean HS image \mathbf{u} and the sparse noise \mathbf{s} for noise-robust restoration. The first and second constraints measure data fidelities to the observation \mathbf{v} and the sparse noise \mathbf{s} , respectively. In many methods, data fidelity is included in an objective function, e.g., [6], [17]] and [14], [4]. On the other hand, as mentioned in [15], [16], [28], [35]–[42], such a constraint-type formulation facilitates the parameter setting because one can intuitively set ε via observed information. Since both constraints are closed convex sets, and HSSTV is a convex function, Prob. (6) is a constrained convex optimization problem.

Since HSSTV is not differentiable, and there are multiple hard constraints, we require a suitable iterative algorithm to solve it. In this paper, we adopt ADMM (see Sec. II-C). In what follows, we reformulate Prob. (6) into Prob. (1) to solve it by ADMM.

By using the indicator functions of the constraints, Prob. (6) can be rewritten as

$$\min_{\mathbf{u}} \|\mathbf{A}_\omega \mathbf{u}\|_{1,p} + \iota_{\mathcal{B}_{2,\varepsilon}^{\mathbf{v}}}(\Phi \mathbf{u} + \mathbf{s}) + \iota_{\mathcal{B}_{1,\eta}}(\mathbf{s}) + \iota_{[\mu_{\min}, \mu_{\max}]^{NB}}(\mathbf{u}). \quad (7)$$

Note that from the definition of the indicator function, Prob. (7) exactly equals to Prob. (6). By letting

$$f: \mathbb{R}^{NB} \rightarrow \mathbb{R}^2: \mathbf{u} \mapsto (0, 0), \quad (8)$$

$$g: \mathbb{R}^{5NB+M} \rightarrow \mathbb{R} \cup \{\infty\}: (\mathbf{z}_1, \mathbf{z}_2, \mathbf{z}_3) \mapsto \|\mathbf{z}_1\|_{1,p} + \iota_{\mathcal{B}_{2,\varepsilon}^{\mathbf{v}}}(\mathbf{z}_2) + \iota_{\mathcal{B}_{1,\eta}}(\mathbf{z}_3) + \iota_{[\mu_{\min}, \mu_{\max}]^{NB}}(\mathbf{z}_4), \quad (9)$$

$$\mathbf{G}: \mathbb{R}^{NB} \rightarrow \mathbb{R}^{5NB+2M}: \mathbf{u} \mapsto (\mathbf{A}_\omega \mathbf{u}, \Phi \mathbf{u} + \mathbf{s}, \mathbf{u}). \quad (10)$$

Prob. (7) is reduced to Prob. (1). The resulting algorithm based on ADMM is summarized in Alg. 1.

Algorithm 1: ADMM method for Prob. (6)

input : $\mathbf{z}_1^{(0)}, \mathbf{z}_2^{(0)}, \mathbf{z}_3^{(0)}, \mathbf{z}_4^{(0)}, \mathbf{d}_1^{(0)}, \mathbf{d}_2^{(0)}, \mathbf{d}_3^{(0)}, \mathbf{d}_4^{(0)}$

1 **while** A stopping criterion is not satisfied **do**

2 $\langle \mathbf{u}^{(n+1)}, \mathbf{s}^{(n+1)} \rangle =$
 $\underset{\mathbf{u}, \mathbf{s}}{\operatorname{argmin}} \frac{1}{2\gamma} (\|\mathbf{z}_1^{(n)} - \mathbf{A}_\omega \mathbf{u} - \mathbf{d}_1^{(n)}\|^2 + \|\mathbf{z}_2^{(n)} - (\Phi \mathbf{u} + \mathbf{s}) - \mathbf{d}_2^{(n)}\|^2 + \|\mathbf{z}_3^{(n)} - \mathbf{s} - \mathbf{d}_3^{(n)}\|^2 + \|\mathbf{z}_4^{(n)} - \mathbf{u} - \mathbf{d}_4^{(n)}\|^2);$

3 $\mathbf{z}_1^{(n+1)} = \operatorname{prox}_{\gamma \|\cdot\|_{1,p}} (\mathbf{A}_\omega \mathbf{u}^{(n+1)} + \mathbf{d}_1^{(n)});$

4 $\mathbf{z}_2^{(n+1)} = \operatorname{prox}_{\gamma \iota_{\mathcal{B}_{2,\varepsilon}^\vee}} (\Phi \mathbf{u}^{(n+1)} + \mathbf{s}^{(n+1)} + \mathbf{d}_2^{(n)});$

5 $\mathbf{z}_3^{(n+1)} = \operatorname{prox}_{\gamma \iota_{\mathcal{B}_{1,\eta}}} (\mathbf{s}^{(n+1)} + \mathbf{d}_3^{(n)});$

6 $\mathbf{z}_4^{(n+1)} = \operatorname{prox}_{\gamma \iota_{[\mu_{\min}, \mu_{\max}]^{NB}}} (\mathbf{u}^{(n+1)} + \mathbf{d}_4^{(n)});$

7 $\mathbf{d}_1^{(n+1)} = \mathbf{d}_1^{(n)} + \mathbf{A}_\omega \mathbf{u}^{(n+1)} - \mathbf{z}_1^{(n+1)};$

8 $\mathbf{d}_2^{(n+1)} = \mathbf{d}_2^{(n)} + \Phi \mathbf{u}^{(n+1)} + \mathbf{s}^{(n+1)} - \mathbf{z}_2^{(n+1)};$

9 $\mathbf{d}_3^{(n+1)} = \mathbf{d}_3^{(n)} + \mathbf{s}^{(n+1)} - \mathbf{z}_3^{(n+1)};$

10 $\mathbf{d}_4^{(n+1)} = \mathbf{d}_4^{(n)} + \mathbf{u}^{(n+1)} - \mathbf{z}_4^{(n+1)};$

11 $n \leftarrow n + 1;$

The update of \mathbf{u} and \mathbf{s} in Alg. 1 come down to the following forms:

$$\begin{aligned} \mathbf{u}^{(n+1)} &= \left(\mathbf{A}_\omega^\top \mathbf{A}_\omega + \Phi^\top \Phi + \frac{1}{2} \mathbf{I} \right)^{-1} \text{RHS}, \\ \text{RHS} &= \mathbf{A}_\omega^\top (\mathbf{z}_1^{(n)} - \mathbf{d}_1^{(n)}) + \frac{1}{2} \Phi^\top (\mathbf{z}_2^{(n)} - \mathbf{d}_2^{(n)}) \\ &\quad - \frac{1}{2} (\mathbf{z}_3^{(n)} - \mathbf{d}_3^{(n)}) + (\mathbf{z}_4^{(n)} - \mathbf{d}_4^{(n)}), \\ \mathbf{s}^{(n+1)} &= \frac{1}{2} (\mathbf{z}_2^{(n)} - \mathbf{u}^{(n+1)} - \mathbf{d}_2^{(n)} + \mathbf{z}_3^{(n)} - \mathbf{d}_3^{(n)}), \end{aligned} \quad (11)$$

Since the update of \mathbf{u} and \mathbf{s} in Alg. 1 is strictly-convex quadratic minimization, one can obtain this update forms by differentiating it. Here, we should consider the structure of Φ because it affects the matrix inversion in (11). If Φ is a block-circulant-with-circulant-blocks (BCCB) matrix [43], we can leverage 3DFFT to efficiently solve the inversion in Step 2 with the difference operators having periodic boundary, i.e., $\mathbf{A}_\omega^\top \mathbf{A}_\omega + \Phi^\top \Phi + \mathbf{I}$ can be diagonalized by the 3D FFT matrix and its inverse. If Φ is a semi-orthogonal matrix, i.e., $\Phi \Phi^\top = \alpha \mathbf{I}$ ($\alpha > 0$), we leave it to the update of \mathbf{z}_2 , which means that we replace $\iota_{\mathcal{B}_{2,\varepsilon}^\vee}$ by $\iota_{\mathcal{B}_{2,\varepsilon}^\vee} \circ \Phi$ in (9) and $\Phi \mathbf{u}$ by \mathbf{u} in (10). This is because the proximity operator of $\iota_{\mathcal{B}_{2,\varepsilon}^\vee} \circ \Phi$ in this case can be computed by using [44, Table 1.1-x] as follows:

$$\operatorname{prox}_{\gamma \iota_{\mathcal{B}_{2,\varepsilon}^\vee} \circ \Phi}(\mathbf{x}) = \mathbf{x} + \alpha^{-1} \Phi^\top (P_{\mathcal{B}_{2,\varepsilon}^\vee}(\Phi \mathbf{x}) - \Phi \mathbf{x}).$$

If Φ is a sparse matrix, we offer to use a preconditioned conjugate gradient method [45] for approximately solving the inversion, or to apply primal-dual splitting methods [46]–[48] instead of ADMM.³ Otherwise, randomized image restoration methods using stochastic proximal splitting algorithms [49]–[52] might be useful for reducing the computational cost.

For the update of \mathbf{z}_1 , the proximity operators are reduced to simple soft-thresholding type operations: for $\gamma > 0$ and for $i = 1, \dots, 4NB$, (i) in the case of $p = 1$,

$$[\operatorname{prox}_{\gamma \|\cdot\|_1}(\mathbf{x})]_i = \operatorname{sgn}(x_i) \max\{|x_i| - \gamma, 0\},$$

³Primal-dual splitting methods require no matrix inversion but in general their convergence speed is slower than ADMM.

where sgn is the sign function, and (ii) in the case of $p = 2$,

$$[\operatorname{prox}_{\gamma \|\cdot\|_{1,2}}(\mathbf{x})]_i = \max \left\{ 1 - \gamma \left(\sum_{j=0}^3 x_{i+jNB}^2 \right)^{-\frac{1}{2}}, 0 \right\} x_i,$$

where $\tilde{i} := ((i-1) \bmod NB) + 1$.

The update of \mathbf{z}_2 , \mathbf{z}_3 , and \mathbf{z}_4 require the proximity operators of the indicator functions of $\mathcal{B}_{2,\varepsilon}^\vee$, $\mathcal{B}_{1,\eta}$ and $[\mu_{\min}, \mu_{\max}]^{NB}$, respectively, which equal to the metric projections onto them (see Sec II-B). Specifically, the metric projection onto $\mathcal{B}_{2,\varepsilon}^\vee$ is given by

$$P_{\mathcal{B}_{2,\varepsilon}^\vee}(\mathbf{x}) = \begin{cases} \mathbf{x}, & \text{if } \mathbf{x} \in \mathcal{B}_{2,\varepsilon}^\vee, \\ \mathbf{v} + \frac{\varepsilon(\mathbf{x} - \mathbf{v})}{\|\mathbf{x} - \mathbf{v}\|}, & \text{otherwise,} \end{cases}$$

that onto $\mathcal{B}_{1,\eta}$ is given by

$$P_{\mathcal{B}_{1,\eta}} = \operatorname{sgn}(\mathbf{x}) \max(|\mathbf{x}| - \eta, 0),$$

and that onto $[\mu_{\min}, \mu_{\max}]^{NB}$ is given, for $i = 1, \dots, NB$, by

$$[P_{[\mu_{\min}, \mu_{\max}]^{NB}}(\mathbf{x})]_i = \min\{\max\{x_i, \mu_{\min}\}, \mu_{\max}\}.$$

V. EXPERIMENTS

We demonstrate the advantages of HSSTV by applying it to two specific HS image restoration problems: denoising and CS reconstruction. In these experiments, we use 13 HS images taken from the *SpectTIR* [53], *MultiSpec* [54] and *GIC* [55], where their dynamic range were normalized into $[0, 1]$.

HSSTV is compared with HTV [6], SSTV [14] and ASSTV [15]. For a fair comparison, we replaced HSSTV in Prob. (6) with HTV, SSTV or ASSTV, and solved the problem by ADMM. In the denoising experiment, we also compare HSSTV with Low-Rank Matrix Recovery (LRMR) [33] as a basic LRM-based method. This is because many other methods combine LRM and TV for high-quality restoration, and we expect that HSSTV can achieve higher performance than the methods by replacing existing TVs. Since LRMR is customized to the mixed noise removal problem, we cannot adopt it for CS reconstruction. We do not compare HSSTV with a recent CNN-based HS image denoising method [56]. The CNN-based method cannot be represented as explicit regularization functions and is fully customized to denoising tasks. In contrast, our HSSTV can be used as a building block in various HS image restoration methods based on optimization. Meanwhile, CNN-based methods strongly depend on what training data are used, which means that they cannot adapt to a wide range of noise intensity. Thus, the design concepts of these methods are different from TVs and LRM-based techniques.

To quantitatively evaluate restoration performance, we use the peak signal-to-noise ratio (PSNR) [dB] index and the structural similarity (SSIM) [57] index between a true HS image $\bar{\mathbf{u}}$ and a restored HS image \mathbf{u} . PSNR is defined by $10 \log_{10}(NB/\|\mathbf{u} - \bar{\mathbf{u}}\|^2)$, and the higher the value is, the more similar the two

TABLE II
PSNR (LEFT) AND SSIM (RIGHT) IN MIXED NOISE REMOVAL EXPERIMENTS.

	$(\sigma, s_p, l_v = l_h)$	PSNR[dB]						SSIM					
		HTV	SSTV	ASSTV	LRMR	HSSTV ($p = 1$)	HSSTV ($p = 2$)	HTV	SSTV	ASSTV	LRMR	HSSTV ($p = 1$)	HSSTV ($p = 2$)
Beltsville	(0.05, 0.04, 0.04)	29.43	33.66	27.16	30.91	34.25	34.16	0.7902	0.8856	0.8111	0.8583	0.9132	0.9085
256 × 256 × 32	(0.1, 0.05, 0.05)	26.40	28.42	24.60	27.13	29.79	29.62	0.6954	0.7057	0.7177	0.7083	0.8186	0.8088
Suwannee	(0.05, 0.04, 0.04)	30.14	34.59	32.60	30.30	35.15	36.01	0.8406	0.9353	0.9052	0.8689	0.9559	0.9555
256 × 256 × 32	(0.1, 0.05, 0.05)	26.70	29.55	28.71	26.90	31.08	31.22	0.7542	0.8146	0.8226	0.7470	0.9125	0.9158
DC	(0.05, 0.04, 0.04)	26.46	33.03	28.80	31.71	33.36	33.08	0.7622	0.9274	0.8676	0.9248	0.9442	0.9394
256 × 256 × 32	(0.1, 0.05, 0.05)	23.84	27.71	25.25	27.35	28.57	28.32	0.6189	0.8092	0.7211	0.8214	0.8611	0.8533
Cuprite	(0.05, 0.04, 0.04)	31.67	34.42	29.14	30.16	34.96	36.20	0.8550	0.9179	0.8632	0.8495	0.9459	0.9426
256 × 256 × 32	(0.1, 0.05, 0.05)	28.20	29.86	26.57	27.32	31.63	31.73	0.7849	0.7717	0.7953	0.7098	0.9031	0.9058
Reno	(0.05, 0.04, 0.04)	28.53	34.37	30.49	32.21	35.11	34.96	0.7818	0.9322	0.8832	0.9012	0.9531	0.9515
256 × 256 × 32	(0.1, 0.05, 0.05)	25.56	28.11	26.95	28.47	29.83	29.72	0.6640	0.8045	0.7539	0.7905	0.8679	0.8635
Botswana	(0.05, 0.04, 0.04)	27.98	33.32	26.47	31.62	33.61	33.53	0.7896	0.9202	0.8199	0.9068	0.9343	0.9344
256 × 256 × 32	(0.1, 0.05, 0.05)	25.21	28.55	24.01	28.31	29.39	29.35	0.6810	0.8175	0.7095	0.8201	0.8745	0.8765
IndianPines	(0.05, 0.04, 0.04)	31.05	31.45	29.07	28.96	31.90	31.80	0.8118	0.8015	0.7671	0.7593	0.8335	0.8243
145 × 145 × 32	(0.1, 0.05, 0.05)	28.57	27.82	26.72	26.15	29.26	29.18	0.7713	0.6229	0.7303	0.6104	0.7785	0.7689
KSC	(0.05, 0.04, 0.04)	30.17	34.74	31.64	33.74	36.39	36.33	0.8271	0.9116	0.8922	0.8890	0.9542	0.9532
256 × 256 × 32	(0.1, 0.05, 0.05)	28.03	29.23	28.62	30.19	31.82	31.72	0.7598	0.7885	0.8064	0.7529	0.8809	0.8747
PaviaLeft	(0.05, 0.04, 0.04)	27.62	35.57	30.91	33.01	35.98	35.81	0.7752	0.9593	0.8828	0.9359	0.9661	0.9645
216 × 216 × 32	(0.1, 0.05, 0.05)	24.74	29.93	26.71	29.46	30.47	30.24	0.6102	0.8755	0.7267	0.8565	0.8898	0.8815
PaviaRight	(0.05, 0.04, 0.04)	26.93	34.54	31.13	33.33	35.68	35.23	0.7769	0.9494	0.8862	0.9256	0.9616	0.9598
256 × 256 × 32	(0.1, 0.05, 0.05)	24.90	30.70	27.23	29.82	31.59	31.39	0.6474	0.8635	0.7493	0.8261	0.9086	0.9006
PaviaU	(0.05, 0.04, 0.04)	27.92	35.52	31.65	33.00	36.31	36.17	0.7973	0.9452	0.8891	0.9124	0.9622	0.9610
256 × 256 × 32	(0.1, 0.05, 0.05)	25.24	30.21	27.42	29.43	31.04	30.80	0.6776	0.8444	0.7678	0.8103	0.8935	0.8855
Salinas	(0.05, 0.04, 0.04)	32.59	35.86	32.83	31.82	37.60	37.65	0.8997	0.9015	0.9163	0.8270	0.9561	0.9564
217 × 217 × 32	(0.1, 0.05, 0.05)	28.88	28.19	28.99	28.02	32.01	32.12	0.8570	0.7117	0.8732	0.6670	0.9223	0.9240
SalinaA	(0.05, 0.04, 0.04)	32.54	35.29	28.12	31.18	36.27	36.23	0.9129	0.9134	0.8468	0.8632	0.9448	0.9416
83 × 86 × 32	(0.1, 0.05, 0.05)	28.69	29.67	25.19	27.67	31.68	31.64	0.8793	0.7789	0.8110	0.7266	0.9197	0.9195

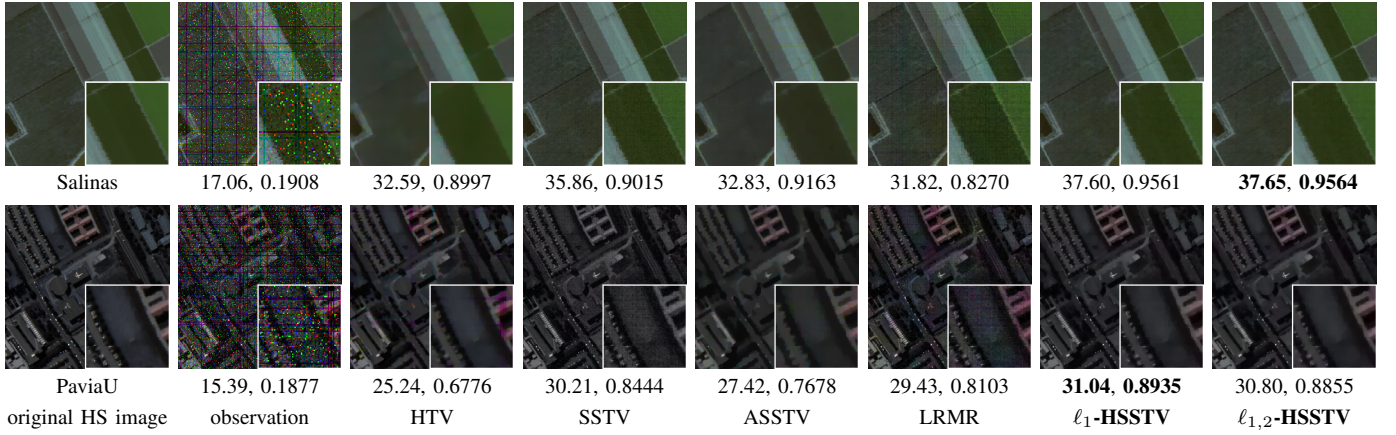


Fig. 3. Resulting HS images with their PSNR (left) and SSIM (right) in the mixed noise removal experiment (top: Salinas, $(\sigma, s_p, l_v = l_h) = (0.05, 0.04, 0.04)$, bottom: PaviaU, $(0.1, 0.05, 0.05)$).

images are. SSIM is an image quality assessment index based on the human vision system, which is defined as follows:

$$SSIM(\mathbf{u}, \bar{\mathbf{u}}) = \frac{1}{P} \sum_{i=1}^P SSIM_i(\mathbf{u}, \bar{\mathbf{u}}),$$

$$SSIM_i(\mathbf{u}, \bar{\mathbf{u}}) = \frac{(2\mu_{\mathbf{u}_i}\mu_{\bar{\mathbf{u}}_i} + C_1)(2\sigma_{\mathbf{u}_i\bar{\mathbf{u}}_i} + C_2)}{(\mu_{\mathbf{u}_i}^2 + \mu_{\bar{\mathbf{u}}_i}^2 + C_1)(\sigma_{\mathbf{u}_i}^2 + \sigma_{\bar{\mathbf{u}}_i}^2 + C_2)},$$

where \mathbf{u}_i and $\bar{\mathbf{u}}_i$ are the i th pixel-centered local patches of a restored HS image and a true HS image, respectively, P is the number of patches, $\mu_{\mathbf{u}_i}$ and $\mu_{\bar{\mathbf{u}}_i}$ is the average values of the local patches of the restored and true HS images, respectively, $\sigma_{\mathbf{u}_i}$ and $\sigma_{\bar{\mathbf{u}}_i}$ represent the variances of \mathbf{u}_i and $\bar{\mathbf{u}}_i$, respectively, and $\sigma_{\mathbf{u}_i\bar{\mathbf{u}}_i}$ denotes the covariance between \mathbf{u}_i and $\bar{\mathbf{u}}_i$. Moreover, C_1 and C_2 are two constants, which avoid the numerical instability when either $\mu_{\mathbf{u}_i}^2 + \mu_{\bar{\mathbf{u}}_i}^2$ or $\sigma_{\mathbf{u}_i}^2 + \sigma_{\bar{\mathbf{u}}_i}^2$ is very close to zero. SSIM gives a normalized score between

zero and one, where the maximum value means that \mathbf{u} equals to $\bar{\mathbf{u}}$.

We set the max iteration number, the stepsize γ and the stopping criterion of ADMM to 5000, 0.1 and $\|\mathbf{u}^{(n)} - \mathbf{u}^{(n+1)}\| < 0.01$, respectively.

A. Mixed Noise Removal

First, we experimented on gaussian-sparse mixed noise removal of HS images, where observed HS images included an additive white Gaussian noise \mathbf{n} with the standard deviation σ and sparse noise \mathbf{s} . In these experiments, we assume sparse noise consists of salt-and-pepper noise, and vertical and horizontal line noise with these noise ratio in all pixels is s_p , l_v , and l_h . We generated noisy HS images by adding two types of mixed noise with $(\sigma, s_p, l_v = l_h) = (0.05, 0.04, 0.04)$ and $(0.1, 0.05, 0.05)$ to true HS images. In this case, $\Phi = \mathbf{I}$ in (5), and the radiuses ε and η in Prob. (6) were set

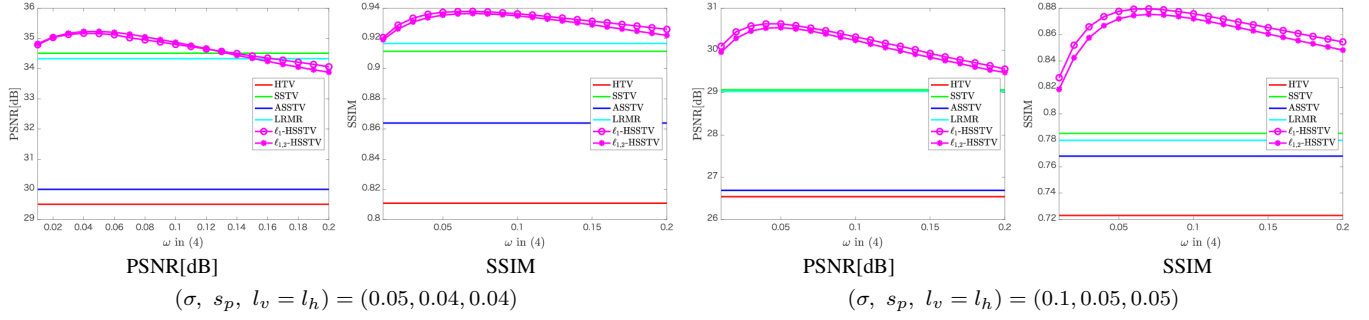
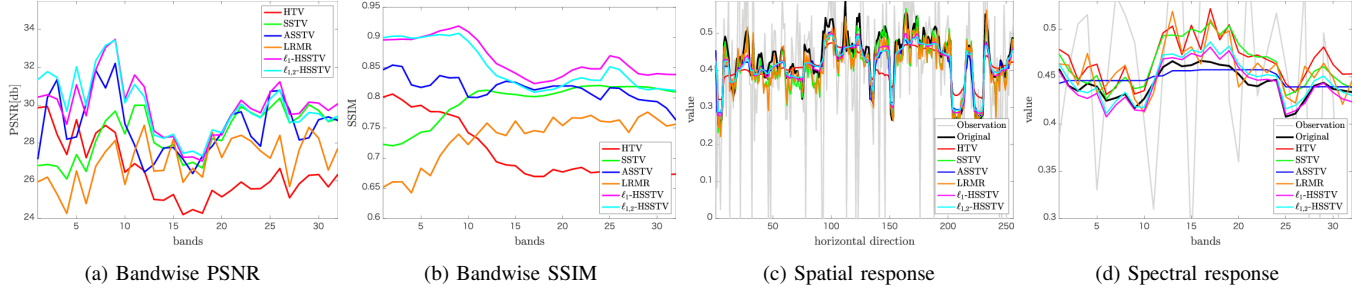
Fig. 4. PSNR or SSIM versus ω in (4) in the mixed noise removal experiment.

Fig. 5. Bandwise PSNR and SSIM and spatial and spectral responses in the mixed noise removal experiment (Suwannee).

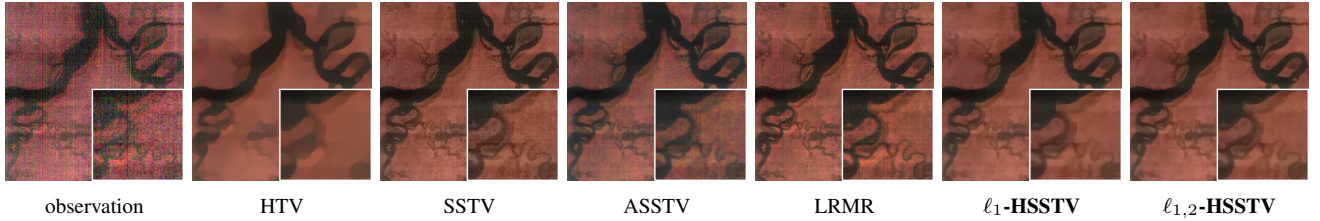


Fig. 6. Resulting HS images on the real noise removal experiment.

to $0.83\sqrt{NB(1-(s_p(1-l_v-l_h)+l_v+l_h-l_vl_h))\sigma^2}$ and $NB(0.45s_p+(l_v+l_h)v_{ave}-l_vl_hv_{ave})$, respectively, where v_{ave} is the average of the observed image. We set the weights in ASSTV $\tau_v = \tau_h = 1$ with both noise intensity. The parameter τ_b was experimentally set to the better value, i.e., $\tau_b = 3$ in the case of $(\sigma, s_p, l_v = l_h) = (0.05, 0.04, 0.04)$ and $\tau_b = 2$ in the case of $(0.1, 0.05, 0.05)$. In LRMR, the upper rank was set to $r = 3$, and we set the upper card as the rate of sparse noise. The parameter settings enable the methods to achieve the best performance.

In Tab. II, we show PSNR and SSIM of the denoised HS images by each method for two types of noise intensity and HS images. The balancing weight ω in HSSTV is set to 0.04. For all HS images, noise intensity, and quality measures, HSSTV outperforms the existing methods. We also found that SSTV does not work well when noise intensity is large. On the other hand, HSSTV is effective for a wide range of noise intensity. This would be because HSSTV simultaneously evaluates spatio-spectral piecewise-smoothness and direct spatial one.

Fig. 3 shows the resulting images on *Salinas* ($(\sigma, s_p, l_v = l_h) = (0.05, 0.04, 0.04)$, top) and *PaviaU* ($(\sigma, s_p, l_v = l_h) = (0.1, 0.05, 0.05)$, bottom) with their PSNR (left) and SSIM (right). Here, we depict these HS images as RGB images ($R =$

8th, $G = 16$ th and $B = 32$ nd bands). One can see that the results by HTV and ASSTV lose spacial details, and noise remains in the results by SSTV and LRMR. Besides, since the restored image by SSTV loses color with large noise intensity, SSTV changes spectral variation. In contrast, HSSTV can restore HS images preserving both details and spectral information without artifacts.

Fig. 4 plots PSNR or SSIM of the results by HSSTV versus various ω in (4) changed from 0.01 to 0.2, where the values of PSNR and SSIM are averaged over the 13 HS images. One can see that $\omega \in [0.03, 0.07]$ is a good choice in most cases. ASSTV requires to newly adjust the parameters τ_v , τ_h , and τ_b for difference noise intensity, but the suitable parameter ω in HSSTV is noise-robust.

Fig. 5 plots bandwise PSNR and SSIM (left) and spatial and spectral responses (right) of the denoised *Suwannee* HS image, where $(\sigma, s_p, l_v = l_h) = (0.1, 0.05, 0.05)$. The graphs regarding bandwise PSNR and SSIM show that HSSTV achieves higher-quality restoration than HTV and SSTV for all bands and ASSTV and LRMR for most bands. The graph (c) plots the spatial response of the 243rd row of the 30th band. In the same way, the graph (d) plots the spectral response of the 243rd row and 107th col. We can see that the spatial response

TABLE III
PSNR (LEFT) AND SSIM (RIGHT) IN THE CS RECONSTRUCTION EXPERIMENT.

	σ	r	PSNR					SSIM				
			HTV	SSTV	ASSTV	ℓ_1 -HSSTV	$\ell_{1,2}$ -HSSTV	HTV	SSTV	ASSTV	ℓ_1 -HSSTV	$\ell_{1,2}$ -HSSTV
Beltsville	0.1	0.6	27.46	27.53	26.51	31.15	30.71	0.6829	0.6013	0.6836	0.8105	0.7948
		0.8	26.23	24.34	24.12	29.63	29.18	0.6363	0.4348	0.6108	0.7604	0.7427
Suwannee	0.1	0.6	27.97	28.49	27.68	32.98	33.04	0.7332	0.7377	0.7367	0.8902	0.8909
		0.8	26.47	25.69	25.39	31.37	31.44	0.6810	0.5739	0.6633	0.8531	0.8534
DC	0.1	0.6	24.69	27.33	24.71	29.70	29.29	0.6096	0.7522	0.6245	0.8577	0.8460
		0.8	23.31	24.16	22.69	27.98	27.59	0.5215	0.6120	0.5037	0.7970	0.7846
Cuprite	0.1	0.6	29.94	28.21	28.59	34.36	34.34	0.7665	0.6826	0.7652	0.8882	0.8895
		0.8	28.77	25.79	26.38	32.97	32.95	0.7368	0.5057	0.7207	0.8568	0.8578
Reno	0.1	0.6	26.99	27.82	26.49	31.80	31.61	0.6769	0.7414	0.6730	0.8733	0.8705
		0.8	25.57	25.57	24.52	30.22	30.04	0.6202	0.6276	0.5940	0.8263	0.8228
Botswana	0.1	0.6	26.10	27.81	25.13	30.32	30.15	0.6683	0.7551	0.6460	0.8563	0.8598
		0.8	24.66	24.79	22.86	28.79	28.63	0.6014	0.6225	0.5519	0.8119	0.8163
IndianPines	0.1	0.6	30.54	27.65	29.55	31.36	31.04	0.7497	0.5066	0.7617	0.7806	0.7655
		0.8	29.99	25.11	28.19	30.71	30.46	0.7366	0.3488	0.7465	0.7589	0.7491
KSC	0.1	0.6	29.30	28.34	28.63	34.10	34.03	0.7660	0.6814	0.7544	0.9019	0.9002
		0.8	28.11	27.00	26.59	32.67	32.60	0.7318	0.6008	0.7032	0.8698	0.8679
PaviaLeft	0.1	0.6	25.66	29.66	25.41	31.96	31.83	0.6082	0.8386	0.5932	0.8900	0.8857
		0.8	24.26	27.17	23.24	30.20	30.08	0.5103	0.7319	0.4434	0.8418	0.8364
PaviaRight	0.1	0.6	25.83	29.86	25.61	32.45	32.21	0.6357	0.7962	0.6275	0.8937	0.8877
		0.8	24.30	27.54	23.61	30.56	30.38	0.5502	0.6917	0.5069	0.8475	0.8392
PaviaU	0.1	0.6	26.49	30.02	26.38	32.88	32.70	0.6867	0.7830	0.6818	0.8950	0.8901
		0.8	24.95	27.35	24.08	31.13	30.96	0.6138	0.6623	0.5680	0.8557	0.8508
Salinas	0.1	0.6	31.19	27.69	30.18	35.43	35.51	0.8577	0.6153	0.8566	0.9222	0.9245
		0.8	29.94	25.28	28.09	34.05	34.10	0.8404	0.4620	0.8302	0.9052	0.9080
SalinasA	0.1	0.6	30.67	27.93	28.19	34.45	34.14	0.8647	0.6595	0.8489	0.9178	0.9208
		0.8	28.68	24.15	24.94	32.71	32.36	0.8387	0.4810	0.8005	0.8966	0.9002

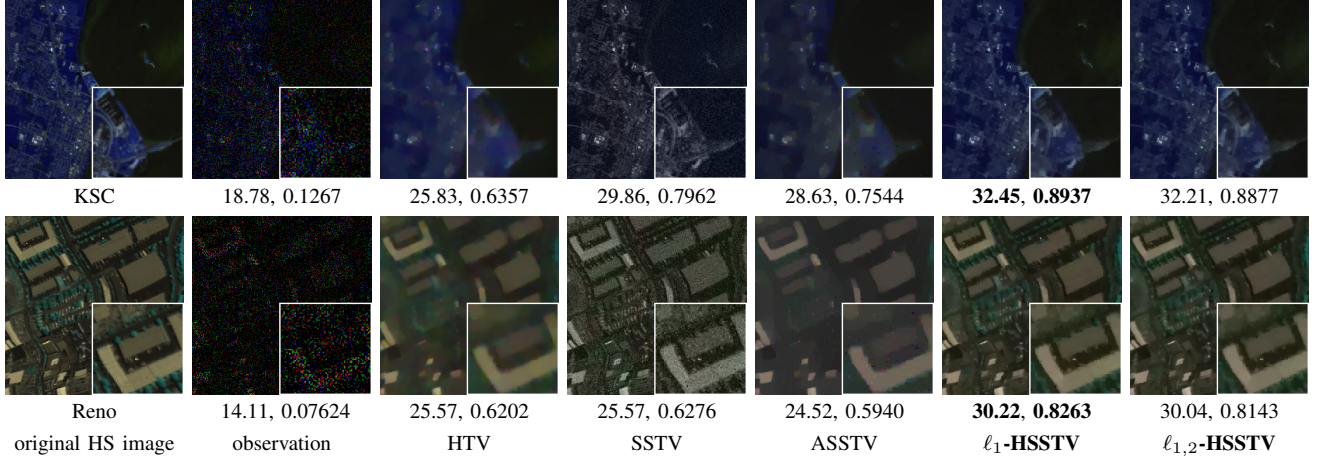


Fig. 7. Resulting HS images with their PSNR (left) and SSIM (right) on the CS reconstruction experiment (top: KSC, $r = 0.4$, bottom: Reno, $r = 0.2$).

of the results by HTV is too smooth compared with the true one. On the other hand, there exist undesirable variations in the spatial response of the result by SSTV and LRMR. In contrast, ASSTV and HSSTV restore similar responses to the true one. In the graph (d), one can see that (i) HTV and LRMR produce spectral artifacts, (ii) the shape of the spectral responses of the results by SSTV is similar to the that of true one, but the mean values are larger than the true one, (iii) the spectral response of the results by ASSTV is too smooth and different from the true one, and (vi) HSSTV can restore a spectral response very similar to the true one.

B. Real Noise Removal

We also examine HTV, SSTV, ASSTV, LRMR, and HSSTV on an HS image with real noise. We selected noisy 16 bands from *Suwannee* and use it as a real observed HS image \mathbf{v} . To maximize the performance of each method, we searched for suitable values of σ , s_p , l_v , and l_h , and we set the parameters as with Sec. V. A. Specifically, we set the parameter $\varepsilon = 3.1893$ and $\eta = 31893$ for all TVs, the parameters τ_v , τ_h , and τ_b are set like Sec. V. A for ASSTV, and the upper rank and the upper card in LRMR are set as 3 and 0.1204, respectively.

Fig 6 shows the results, where the HS images are depicted as RGB images (R = 2nd, G = 6th and B = 13rd bands). The result by HTV has spatial oversmoothing, and SSTV, ASSTV, and LRMR produce spatial artifacts. In addition, one can see that

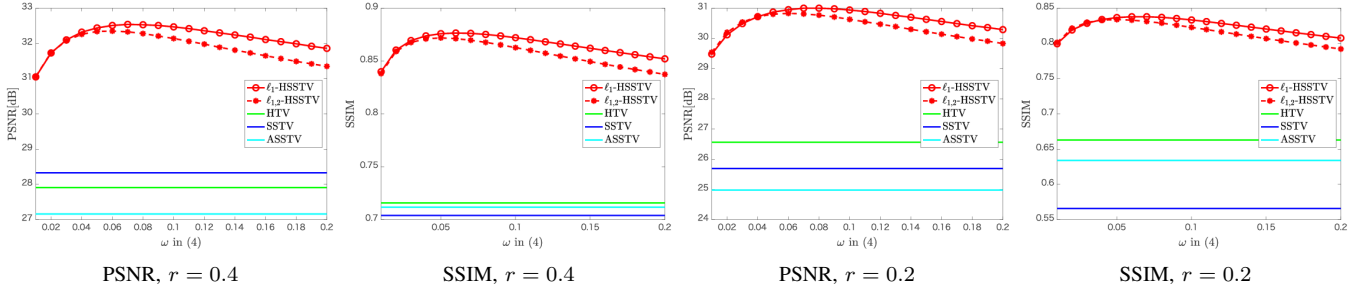
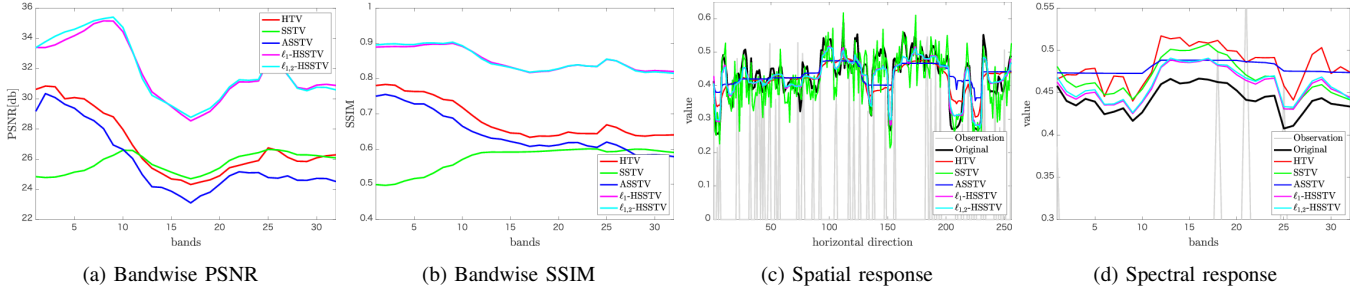
Fig. 8. PSNR or SSIM versus ω in (4) on the CS reconstruction experiment.

Fig. 9. Bandwise PSNR and SSIM and spatial and spectral responses on the CS reconstruction experiment (Suwannee).

the result by LRMR has spectral artifacts. In contrast, HSSTV can restore a detail-preserved HS image without artifacts.

C. Compressed Sensing Reconstruction

We conducted on an experiment on compressed sensing (CS) reconstruction [58], [59]. The CS theory says that high-dimensional signal information can be reconstructed from incomplete random measurements by exploiting some sparsity. In general, HS imaging captures an HS image by scanning 1D spatial and spectral information, because it senses spectral one by dispersing the incident light. Therefore, shooting an HS image spends much time, and so capturing moving objects is very difficult in HS imaging. To overcome the drawback, one-shot HS imaging based on CS has been actively studied [4], [5].

In this experiment, we assume that $\Phi \in \mathbb{R}^{M \times NB}$ in (5) is a random sampling matrix with the sampling rate r ($0 < r < 1$ and $M = rNB$). Here, since Φ is a semi-orthogonal matrix, we can efficiently solve the problem as explained in Sec. IV-B. Moreover, since the main object in the experiments is to verify CS reconstruction performance by HSSTV, we assume that the observations are contaminated by only an additive white Gaussian noise \mathbf{n} with noise intensity $\sigma = 0.1$.

We set the CS reconstruction problem as follows:

$$\min_{\mathbf{u}} \text{HSSTV}(\mathbf{u}) \text{ s.t. } \begin{cases} \Phi \mathbf{u} \in \mathcal{B}_{2,\varepsilon}^y, \\ \mathbf{u} \in [\mu_{\min}, \mu_{\max}]^{NB}. \end{cases}$$

The problem is derived by removing the second constraint and \mathbf{s} from Prob. (6). Therefore, we can solve the above problem by removing \mathbf{s} , \mathbf{z}_3 , and \mathbf{d}_3 in Alg. (1) and replacing \mathbf{z}_4 and \mathbf{d}_4 with \mathbf{z}_3 and \mathbf{d}_3 , respectively. As in Sec. IV-B, the update of

\mathbf{u} is strictly-convex quadratic minimization, and so it comes down to

$$\mathbf{u}^{(n+1)} = (\mathbf{A}_\omega^\top \mathbf{A}_\omega + \Phi^\top \Phi + \mathbf{I})^{-1} \text{RHS},$$

$$\text{RHS} = \mathbf{A}_\omega (\mathbf{z}_1^{(n)} - \mathbf{d}_1^{(n)}) + \Phi^\top (\mathbf{z}_2^{(n)} - \mathbf{d}_2^{(n)}) + (\mathbf{z}_3^{(n)} - \mathbf{d}_3^{(n)}).$$

We set $r = 0.2$ or 0.4 and $\varepsilon = \sqrt{rNB\sigma^2}$. In the ASSTV case, we set the parameters $(\tau_v, \tau_h, \tau_b) = (1, 1, 0.5)$, which experimentally achieves the best performance.

Tab. III shows PSNR and SSIM of the reconstructed HS images. For all r and HS images, both PSNR and SSIM of the results by HSSTV are higher than that by HTV, SSTV, and ASSTV.

Fig. 7 is the reconstructed results on *KSC* and *Reno* with the random sampling ratio $r = 0.4$ and 0.2 , respectively. Here, the HS images are depicted as RGB images ($R = 8\text{th}$, $G = 16\text{th}$ and $B = 32\text{nd}$ bands). One can see that (i) HTV causes spatial oversmoothing, (ii) SSTV produces artifacts and spectral distortion, where it appears as the difference from the color of the true HS images, and (iii) the results by ASSTV have spatial oversmoothing and spectral distortion. On the other hand, HSSTV reconstructs meaningful details without both artifacts and spectral distortion.

Fig. 8 plots PSNR or SSIM of the results by HSSTV versus ω averaged over the 13 HS images for each r . The graphs show that $\omega \in [0.05, 0.1]$ is a good choice in most cases. In comparison with Fig. (4), the suitable range of ω in CS reconstruction is almost the same as that in denoising.

Fig. 9 plots bandwise PSNR or SSIM (left) and spatial and spectral responses (right) (*Suwannee*, $r = 0.2$). According to bandwise PSNR and SSIM, one can see that HSSTV achieves higher-quality reconstruction for all bands than HTV, SSTV, and ASSTV. The graphs (c) and (d) plot the spatial and spectral responses of the same position in Sec. V-A.

The graph (c) shows that (i) the spatial response of the results by HTV and ASSTV are oversmoothing, (ii) SSTV produces undesirable variation, and (iii) the spatial response reconstructed by HSSTV is similar to the true one. In the graph (d), HTV generates undesirable variation, and ASSTV causes oversmoothing. Thanks to the evaluation of spatio-spectral piecewise-smoothness, SSTV reconstructs a similar spectral response to the true one, but the mean values are larger than the true one. HSSTV achieves the most similar reconstruction of spectral response among all the TVs.

VI. CONCLUSION

We have proposed a new TV regularization technique for HS image restoration, named HSSTV. It evaluates both the direct spatial and spatio-spectral piecewise-smoothness of an HS image, leading to an effective regularization for HS images. We also formulate HSSTV-regularized HS restoration as a constrained convex optimization problem and develop an efficient algorithm based on ADMM for solving the problem. Experimental results on mixed noise removal, real noise removal, and CS reconstruction demonstrate the effectiveness and utility of HSSTV.

In this paper, we have focused on a single use of HSSTV. Finally, we would like to note that our HSSTV can be combined with other regularization techniques, for example, LRM and texture regularization [60], [61].

ACKNOWLEDGMENT

The work was partially supported by JSPS Grants-in-Aid (18J20290, 17K12710, 16K12457) and JST-PRESTO.

REFERENCES

- [1] C. I. Chang, *Hyperspectral imaging: techniques for spectral detection and classification*. Springer Science & Business Media, 2003, vol. 1.
- [2] A. P. et al., "Recent advances in techniques for hyperspectral image processing," *Remote sensing of environment*, vol. 113, pp. S110–S122, 2009.
- [3] B. Rasti, P. Scheunders, P. Ghamisi, G. Licciardi, and J. Chanussot, "Noise reduction in hyperspectral imagery: Overview and application," *Remote Sens.*, vol. 10, no. 3, p. 482, 2018.
- [4] R. M. Willett, M. F. Duarte, M. A. Davenport, and R. G. Baraniuk, "Sparsity and structure in hyperspectral imaging: Sensing, reconstruction, and target detection," *IEEE Signal Process. Magazine*, vol. 31, no. 1, pp. 116–126, 2014.
- [5] G. R. Arce, D. J. Brady, L. Carin, H. Arguello, and D. S. Kittle, "Compressive coded aperture spectral imaging: An introduction," *IEEE Signal Process. Magazine*, vol. 31, no. 1, pp. 105–115, 2014.
- [6] Q. Yuan, L. Zhang, and H. Shen, "Hyperspectral image denoising employing a spectral-spatial adaptive total variation model," *IEEE Trans. Geosci. Remote Sens.*, vol. 50, no. 10, pp. 3660–3677, 2012.
- [7] P. Addesso, M. D. Mura, L. Condat, R. Restaino, G. Vivone, D. Picone, and J. Chanussot, "Hyperspectral image inpainting based on collaborative total variation," in *Proc. IEEE Int. Conf. Image Process. (ICIP)*, 2017, pp. 4282–4286.
- [8] X. Zheng, Y. Yuan, and X. Lu, "Hyperspectral image denoising by fusing the selected related bands," *IEEE Trans. Geosci. Remote Sens.*, vol. 57, no. 5, pp. 2596 – 2609, 2018.
- [9] S. Lefkimmatis and A. R. P. M. M. Unser, "Structure tensor total variation," *SIAM J. Imag. Sci.*, vol. 8, no. 2, pp. 1090–1122, 2015.
- [10] H. Liu, P. Sun, Q. Du, Z. Wu, and Z. Wei, "Hyperspectral image restoration based on low-rank recovery with a local neighborhood weighted spectral-spatial total variation model," *IEEE Trans. Geosci. Remote Sens.*, vol. 57, no. 3, pp. 1–14, 2018.
- [11] S. Lefkimmatis and S. Osher, "Nonlocal structure tensor functionals for image regularization," *IEEE Trans. Comput. Imag.*, vol. 1, no. 1, pp. 16–29, 2015.
- [12] G. Chierchia, N. Pustelnik, B. Pesquet-Popescu, and J.-C. Pesquet, "A nonlocal structure tensor-based approach for multicomponent image recovery problems," *IEEE Trans. Image Process.*, vol. 23, no. 12, pp. 5531–5544, 2014.
- [13] S. Ono, K. Shirai, and M. Okuda, "Vectorial total variation based on arranged structure tensor for multichannel image restoration," in *Proc. IEEE Int. Conf. Acoust., Speech, Signal Process. (ICASSP)*, 2016, pp. 4528–4532.
- [14] H. K. Aggarwal and A. Majumdar, "Hyperspectral image denoising using spatio-spectral total variation," *IEEE Geosci. Remote Sens. Lett.*, vol. 13, no. 3, pp. 442–446, 2016.
- [15] W. He, H. Zhang, H. Shen, and L. Zhang, "Hyperspectral image denoising using local low-rank matrix recovery and global spatial-spectral total variation," *IEEE Selected Topics Appl. Earth Obser. Remote Sens.*, vol. 11, no. 3, pp. 713–729, 2018.
- [16] W. He, H. Zhang, L. Zhang, and H. Shen, "Total-variation-regularized low-rank matrix factorization for hyperspectral image restoration," *IEEE Trans. Geosci. Remote Sens.*, vol. 54, no. 1, pp. 178–188, 2016.
- [17] H. K. Aggarwal and A. Majumdar, "Hyperspectral unmixing in the presence of mixed noise using joint-sparsity and total variation," *IEEE Selected Topics Appl. Earth Obser. Remote Sens.*, vol. 9, no. 9, pp. 4257–4266, 2016.
- [18] H. Li, P. Sun, H. Liu, Z. Wu, and Z. Wei, "Non-convex low-rank approximation for hyperspectral image recovery with weighted total variation regularization," in *Proc. IEEE Int. Geosci. Remote Sens. Symp. (IGARSS)*, 07 2018, pp. 2733–2736.
- [19] W. Cao, K. Wang, G. Han, J. Yao, and A. Cichocki, "A robust pca approach with noise structure learning and spatial-spectral low-rank modeling for hyperspectral image restoration," *IEEE Selected Topics Appl. Earth Obser. Remote Sens.*, vol. 11, no. 10, pp. 3863–3879, 2018.
- [20] Y. Wang, J. Peng, Q. Zhao, Y. Leung, X. Zhao, and D. Meng, "Hyperspectral image restoration via total variation regularized low-rank tensor decomposition," *IEEE Selected Topics Appl. Earth Obser. Remote Sens.*, vol. 11, no. 4, pp. 1227–1243, 2017.
- [21] Q. Wang, Z. Wu, J. Jin, T. Wang, and Y. Shen, "Low rank constraint and spatial spectral total variation for hyperspectral image mixed denoising," *Signal Processing*, vol. 142, pp. 11–26, 2018.
- [22] L. Sun, T. Zhan, Z. Wu, L. Xiao, and B. Jeon, "Hyperspectral mixed denoising via spectral difference-induced total variation and low-rank approximation," *Remote Sens.*, vol. 10, no. 12, p. 1956, 2018.
- [23] T. Ince, "Hyperspectral image denoising using group low-rank and spatial-spectral total variation," *IEEE Access*, vol. 7, pp. 52 095–52 109, 2019.
- [24] D. Gabay and B. Mercier, "A dual algorithm for the solution of nonlinear variational problems via finite elements approximations," *Comput. Math. Appl.*, vol. 2, pp. 17–40, 1976.
- [25] J. Eckstein and D. Bertsekas, "On the Douglas-Rachford splitting method and proximal point algorithm for maximal monotone operators," *Math. Program.*, vol. 55, pp. 293–318, 1992.
- [26] J. Eckstein and D. P. Bertsekas, "On the DouglasRachford splitting method and the proximal point algorithm for maximal monotone operators," *Math. Program.*, vol. 55, no. 1-3, pp. 293–318, 1992.
- [27] S. Boyd, N. Parikh, E. Chu, B. Peleato, and J. Eckstein, "Distributed optimization and statistical learning via the alternating direction method of multipliers," *Foundations and Trends in Machine Learning*, vol. 3, no. 1, pp. 1–122, 2011.
- [28] S. Takeyama, S. Ono, and I. Kumazawa, "Hyperspectral image restoration by hybrid spatio-spectral total variation," *Proc. IEEE Int. Conf. Acoust., Speech, Signal Process. (ICASSP)*, pp. 4586–4590, 2017.
- [29] J. J. Moreau, "Fonctions convexes duales et points proximaux dans un espace hilbertien," *C. R. Acad. Sci. Paris Ser. A Math.*, vol. 255, pp. 2897–2899, 1962.
- [30] X. Bresson and T. F. Chan, "Fast dual minimization of the vectorial total variation norm and applications to color image processing," *Inverse Probl. Imag.*, vol. 2, no. 4, pp. 455–484, 2008.
- [31] J. Duran, M. Moeller, C. Sbert, and D. Cremers, "Collaborative total variation: a general framework for vectorial tv models," *SIAM Ima. Sci.*, vol. 9, no. 1, pp. 116–151, 2016.
- [32] G. Chen and S. Qian, "Denoising of hyperspectral imagery using principal component analysis and wavelet shrinkage," *IEEE Trans. Geosci. Remote Sens.*, vol. 49, no. 3, pp. 973–980, 2011.
- [33] H. Zhang, W. He, L. Zhang, H. Shen, and Q. Yuan, "Hyperspectral image restoration using low-rank matrix recovery," *IEEE Trans. Geosci. Remote Sens.*, vol. 52, no. 8, pp. 4729–4743, 2014.

- [34] H. K. Aggarwal and A. Majumdar, "Mixed gaussian and impulse denoising of hyperspectral images," in *Proc. IEEE Int. Geosci. Remote Sens. Symp. (IGARSS)*, 2015, pp. 429–432.
- [35] M. Afonso, J. Bioucas-Dias, and M. Figueiredo, "An augmented Lagrangian approach to the constrained optimization formulation of imaging inverse problems," *IEEE Trans. Image Process.*, vol. 20, no. 3, pp. 681–695, 2011.
- [36] G. Chierchia, N. Pustelnik, J.-C. Pesquet, and B. Pesquet-Popescu, "Epigraphical projection and proximal tools for solving constrained convex optimization problems," *Signal, Image and Video Process.*, vol. 9, no. 8, pp. 1737–1749, 2015.
- [37] S. Ono and I. Yamada, "Signal recovery with certain involved convex data-fidelity constraints," *IEEE Trans. Signal Process.*, vol. 63, no. 22, pp. 6149–6163, 2015.
- [38] Y. Xie, Y. Qu, D. Tao, W. Wu, Q. Yuan, and W. Zhang, "Hyperspectral image restoration via iteratively regularized weighted Schatten p -norm minimization," *IEEE Trans. Geosci. Remote Sens.*, vol. 54, no. 8, pp. 4642–4659, 2016.
- [39] S. Ono, " L_0 gradient projection," *IEEE Trans. Image Process.*, pp. 1–11, 2017, (in press).
- [40] S. Takeyama, S. Ono, and I. Kumazawa, "Robust and effective hyperspectral pansharpening using spatio-spectral total variation," in *Proc. IEEE Int. Conf. Acoust., Speech, Signal Process. (ICASSP)*, 2018, pp. 1603–1607.
- [41] —, "Hyperspectral pansharpening using noisy panchromatic image," in *Asia-Pacific Signal and Information Processing Association Annual Summit and Conference (APSIPA ASC)*, 2018, pp. 880–885.
- [42] —, "Hyperspectral and multispectral data fusion by a regularization considering," in *Proc. IEEE Int. Conf. Acoust., Speech, Signal Process. (ICASSP)*, 2019, pp. 2152–2156.
- [43] P. C. Hansen, J. G. Nagy, and D. P. O'Leary, *Deblurring Images: Matrices, Spectra, and Filtering*. SIAM, 2006.
- [44] P. L. Combettes and J.-C. Pesquet, "Proximal splitting methods in signal processing," in *Fixed-Point Algorithms for Inverse Problems in Science and Engineering*. Springer-Verlag, 2011, pp. 185–212.
- [45] G. H. Golub and C. F. V. Loan, *Matrix Computations*, 4th ed. Johns Hopkins University Press, 2012.
- [46] A. Chambolle and T. Pock, "A first-order primal-dual algorithm for convex problems with applications to imaging," *J. Math. Imaging and Vision*, vol. 40, no. 1, pp. 120–145, 2010.
- [47] P. L. Combettes and J.-C. Pesquet, "Primal-dual splitting algorithm for solving inclusions with mixtures of composite, Lipschitzian, and parallel-sum type monotone operators," *Set-Valued and Variational Analysis*, vol. 20, no. 2, pp. 307–330, 2012.
- [48] L. Condat, "A primal-dual splitting method for convex optimization involving Lipschitzian, proximable and linear composite terms," *J. Optim. Theory Appl.*, 2013.
- [49] S. Ono, M. Yamagishi, T. Miyata, and I. Kumazawa, "Image restoration using a stochastic variant of the alternating direction method of multipliers," in *Proc. IEEE Int. Conf. Acoust., Speech, Signal Process. (ICASSP)*, 2016.
- [50] A. Chambolle, M. J. Ehrhardt, P. Richtárik, and C.-B. Schönlieb, "Stochastic primal-dual hybrid gradient algorithm with arbitrary sampling and imaging applications," *SIAM J. Optim.*, vol. 28, no. 4, pp. 2783–2808, 2018.
- [51] P. L. Combettes and J.-C. Pesquet, "Stochastic forward-backward and primal-dual approximation algorithms with application to online image restoration," in *Proc. Eur. Signal Process. Conf. (EUSIPCO)*, Aug 2016, pp. 1813–1817.
- [52] S. Ono, "Efficient constrained signal reconstruction by randomized epigraphical projection," in *Proc. IEEE Int. Conf. Acoust., Speech, Signal Process. (ICASSP)*, 2019, pp. 4993–4997.
- [53] "SpecTIR," <http://www.spectir.com/free-data-samples/>.
- [54] "MultiSpec," <https://engineering.purdue.edu/biehl/MultiSpec>.
- [55] "GIC," http://www.ehu.eus/ccwintco/index.php?title=Hyperspectral_Remote_Sensing_Scenes.
- [56] W. Liu and J. Lee, "A 3-d atrous convolution neural network for hyperspectral image denoising," *IEEE Trans. Geosci. Remote Sens.*, 2019.
- [57] Z. Wang, A. C. Bovik, H. R. Sheikh, and E. P. Simoncelli, "Image quality assessment: from error visibility to structural similarity," *IEEE Trans. Image Process.*, vol. 13, no. 4, pp. 600–612, 2004.
- [58] R. G. Baraniuk, "Compressive sensing," *IEEE Signal Process. Magazine*, vol. 24, no. 4, 2007.
- [59] E. Candès and M. Wakin, "An introduction to compressive sampling," *IEEE Signal Process. Magazine*, vol. 25, no. 2, pp. 21–30, 2008.
- [60] H. Schaeffer and S. Osher, "A low patch-rank interpretation of texture," *SIAM J. Imag. Sci.*, vol. 6, no. 1, pp. 226–262, 2013.
- [61] S. Ono, T. Miyata, and I. Yamada, "Cartoon-texture image decomposition using blockwise low-rank texture characterization," *IEEE Trans. Image Process.*, vol. 23, no. 3, pp. 1128–1142, 2014.